Corrosion Science 182 (2021) 109267

Contents lists available at ScienceDirect

Corrosion Science

journal homepage: www.elsevier.com/locate/corsci

Y-Hf co-doped AlCoCrFeNi high-entropy alloy coating with superior oxidation and spallation resistance at 1100 °C

Jie Lu [a], Ling Li [a], Ying Chen [b], Xuanzhen Liu [a], Xiaofeng Zhao [a,*], Fangwei Guo [a], Ping Xiao [a]

[a] Shanghai Key Laboratory of Advanced High-Temperature Materials and Precision Forming, School of Materials Science and Engineering, Shanghai Jiao Tong University, Shanghai, 200240, China
[b] School of Materials, The University of Manchester, MSS Tower, Manchester, M13 9PL, United Kingdom

ARTICLE INFO

Keywords:
High-entropy alloy
AlCoCrFeNi coating
Oxidation
High temperature

ABSTRACT

The oxidation behavior of Y-Hf co-doped AlCoCrFeNi high-entropy alloy coating (HEA coating) at 1100 °C was investigated and compared with that of conventional Y-Hf co-doped NiCoCrAl alloy coating (CNA coating) in this study. First, the HEA coating exhibits an extremely low oxidation rate with an oxidation rate constant of 1.3×10^{-2} μm^2/h, which is 50 % lower than that of CNA coating. Second, the HEA coating shows much better resistance to the oxide scale spallation compared with CNA coating, resulting from the lower oxidation rate and the well suppression of interface rumpling.

1. Introduction

MCrAlY (M = Ni, Co or both) alloys are extensively applied as the bond coats in thermal barrier coatings (TBCs) to protect the Ni-based superalloy components from oxidation at high temperatures [1–6]. The oxidation resistance of these coatings is predominantly achieved by forming a continuous, adherent and slowly growing Al_2O_3 scale on the coating surface upon exposure to high temperatures. A fairly high residual stress (about 3–6 GPa) in a compressively stressed state will develop in the Al_2O_3 scale, mainly due to the thermal expansion misfit of Al_2O_3 with the metal substrate upon cooling to room temperature [7]. The large stress generates the elastic strain energy stored in the Al_2O_3 scale. Then, the elastic strain energy could motivate the scale spallation once a critical thickness is reached, as the elastic strain energy is proportional to the scale thickness [8]. Thus, a low rate of Al_2O_3 scale thickening is of importance to improve resistance to scale spallation and the durability at high temperatures.

Unfortunately, the oxidation rates of MCrAlY alloys are usually one order of magnitude higher than those of the typical Al_2O_3-forming alloys, such as β-NiAlHf and FeCrAlY [9–13]. However, at present, both NiAlHf and FeCrAlY are difficult to be used as the bond coats in TBCs due to their intrinsic shortcomings. First, the high Al content (about 31.4 wt%) in β-NiAlHf causes severe inter-diffusion with the Ni-based superalloy substrate, which leads to the formation of a secondary reaction zone (SRZ). A large amount of brittle topologically close-packed (TCP) phase precipitate from the SRZ, thus resulting in the degradation of creep-rapture resistance of Ni-based superalloy. Therefore, SRZ might cause initiation and propagation of cracks along the grain boundaries in the SRZ [14]. Second, the Al concentration in the β-NiAlHf declines rapidly due to the inter-diffusion with the Ni-based alloy substrate. Once the Al concentration in the β-NiAlHf is less than 17 wt%, the external Al_2O_3 scale growth is difficult to be sustained because of an inadequate Al supply [15]. The FeCrAlY is not practically used for the bond coat because the Al in the coating reacts with the Ni in the Ni-based superalloy to form a NiAl layer between the coating and the alloy substrate at high temperatures [16]. Additionally, the extremely low strength at high temperatures for the FeCrAlY also restricts its high-temperature application [17,18]. It is extensively reported that the high oxidation rates at/above 1100 °C for MCrAlY lead to premature failure of Al_2O_3 scale easily [19–21]. Therefore, to meet the requirements of high stability and long life of TBCs at/above 1100 °C in the future, it is of necessity to develop an ultra oxidation resistant bond coat material at/above 1100 °C with an excellent chemical compatibility with the Ni-based superalloy substrate and an appropriate high-temperature strength.

In this contribution, an ultra oxidation and spallation resistant Y-Hf co-doped AlCoCrFeNi high-entropy alloy at 1100 °C is reported in our recent work [22]. Its oxidation rate is one order of magnitude lower than those of MCrAlY and comparable to those of NiAlHf and FeCrAlY. The mechanical properties of AlCoCrFeNi HEA at high temperatures were

* Corresponding author.
E-mail address: xiaofengzhao@sjtu.edu.cn (X. Zhao).

https://doi.org/10.1016/j.corsci.2021.109267
Received 15 November 2020; Received in revised form 15 January 2021; Accepted 17 January 2021
Available online 20 January 2021

Table 1
Chemical composition of HEA coating and CNA coating.

Phases	Elements (at. %)						
	Al	Co	Cr	Fe	Ni	Y	Hf
HEA coating	19.99	19.99	19.99	19.99	19.99	0.02	0.02
CNA coating	22.37	19.71	16.51	/	41.37	0.02	0.02

investigated by Lim et al. [23]. Their results indicate that the high-temperature yield strength of AlCoCrFeNi is higher than that of conventional NiCoCrAlY [24]. The extremely low oxidation rate, the ultra strong resistance to the oxide scale spallation and the appropriate high-temperature strength of Y-Hf co-doped AlCoCrFeNi high-entropy alloy make it an excellent candidate material as a bond coat in TBCs or an oxidation protective overlay coating at high temperatures.

Up to now, the oxidation behavior of Y-Hf co-doped AlCoCrFeNi high-entropy alloy coating has not been reported and is still unclear. Unlike the oxidation of bulk alloy, the interaction of coating and Ni-based superalloy substrate can change the composition and structure of coating, thus affecting the oxidation behavior of coating [25]. Therefore, it is urgent to understand the oxidation behavior of AlCoCrFeNi high-entropy alloy coating with Y-Hf co-doping and clarify its reliability of the coating application. In this study, a thin plate of Y-Hf co-doped AlCoCrFeNi high-entropy alloy was bonded onto the Ni-based superalloy using spark plasma sintering (SPS) technique to fabricate coating samples. The coatings are typically deposited by air plasma spray (APS), high velocity air fuel (HVAF), vacuum plasma spray (VPS) and electric beam physical vapor deposition (EBPVD) [11,12,26], but the SPS has attracted increasing attention on fabricating model samples for the scientific research, due to its capability of fast sintering. The multilayer TBCs model samples with the MCrAlY bond coats on the Ni-based superalloys have been already fabricated using SPS and the corresponding performances were investigated [27–31]. In our previous works [32–34], NiCoCrAlY or reactive element oxides dispersed β-NiAl coating model samples were also produced by SPS to investigate their oxidation behavior expediently.

The overarching objective of this work is to investigate and understand the oxidation behavior of Y-Hf co-doped AlCoCrFeNi high-entropy alloy coating **(termed as HEA coating)** at 1100 °C. The conventional Y-Hf co-doped NiCoCrAl alloy coating **(termed as CNA coating)** was also fabricated as a counterpart to further reveal the oxidation behavior of HEA coating. The growth of oxide scale, the residual stress in oxide scale, inter-diffusion of coating with superalloy, and the microstructural evolution of coating are investigated in detail to understand the underlying oxidation mechanism of HEA coating comprehensively.

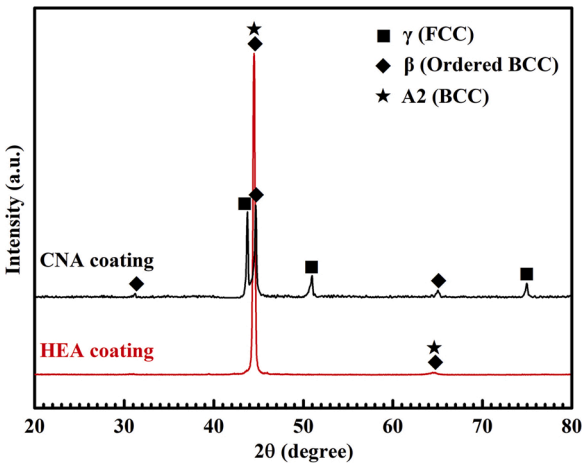

Fig. 2. XRD results of two types of coatings.

2. Experimental procedure

2.1. Material and sample preparation

The Y-Hf co-doped AlCoCrFeNi and NiCoCrAl (referring to Amdry 365-2, Sulzer Metco) were melted in a vacuum induction melting furnace with a mixture of the constituent elements (≥99.9 wt%), as shown in Table 1. The molten alloy was poured into a high-purity graphite crucible. Then the alloy rods were directionally solidified at a constant growth rate of 10 mm/min and cast into the size of 48 mm (diameter) ×120 mm (height). The solidified rods were cut into the

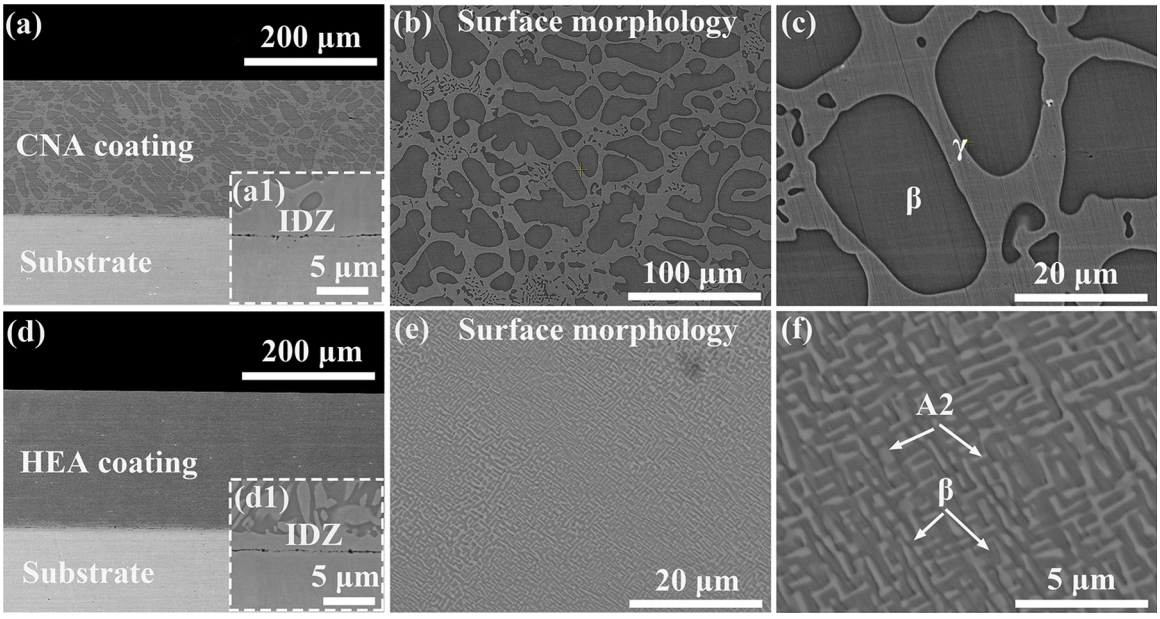

Fig. 1. (a, d) low magnification backscattered SEM (BSE) images, giving an overview of cross-sectional microstructure for the CNA coating and HEA coating, respectively; (a1, d1) high magnification BSE images, showing the inter-diffusion zone (IDZ) of CNA coating and HEA coating, respectively; (b, c) high magnification BSE images of surface morphology, showing the typical two-phase microstructure of CNA coating; (e, f) high magnification BSE images of surface morphology, showing the typical two-phase microstructure of HEA coating.

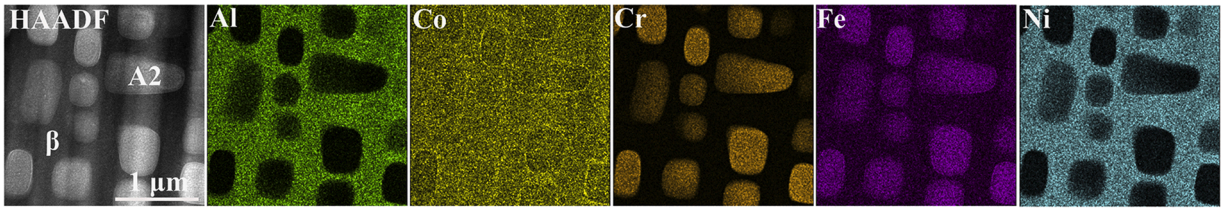

Fig. 3. A high-angle annular dark-field (HAADF) STEM image of HEA coating with corresponding elemental maps, showing the size and chemical composition of A2 and β phases.

circular plates with a size of 45 mm (diameter) × 500 μm (thickness) using a wire cutting machine. The circular plates were subsequently sintered on the nickel-based Hastelloy® X polycrystalline superalloy with a size of 48 mm (diameter) ×5 mm (height) using SPS to produce coating samples. The sintering process was performed at 1050 °C for 20 min under a pressure of 30 MPa in vacuum (10^{-3} Pa). The heating

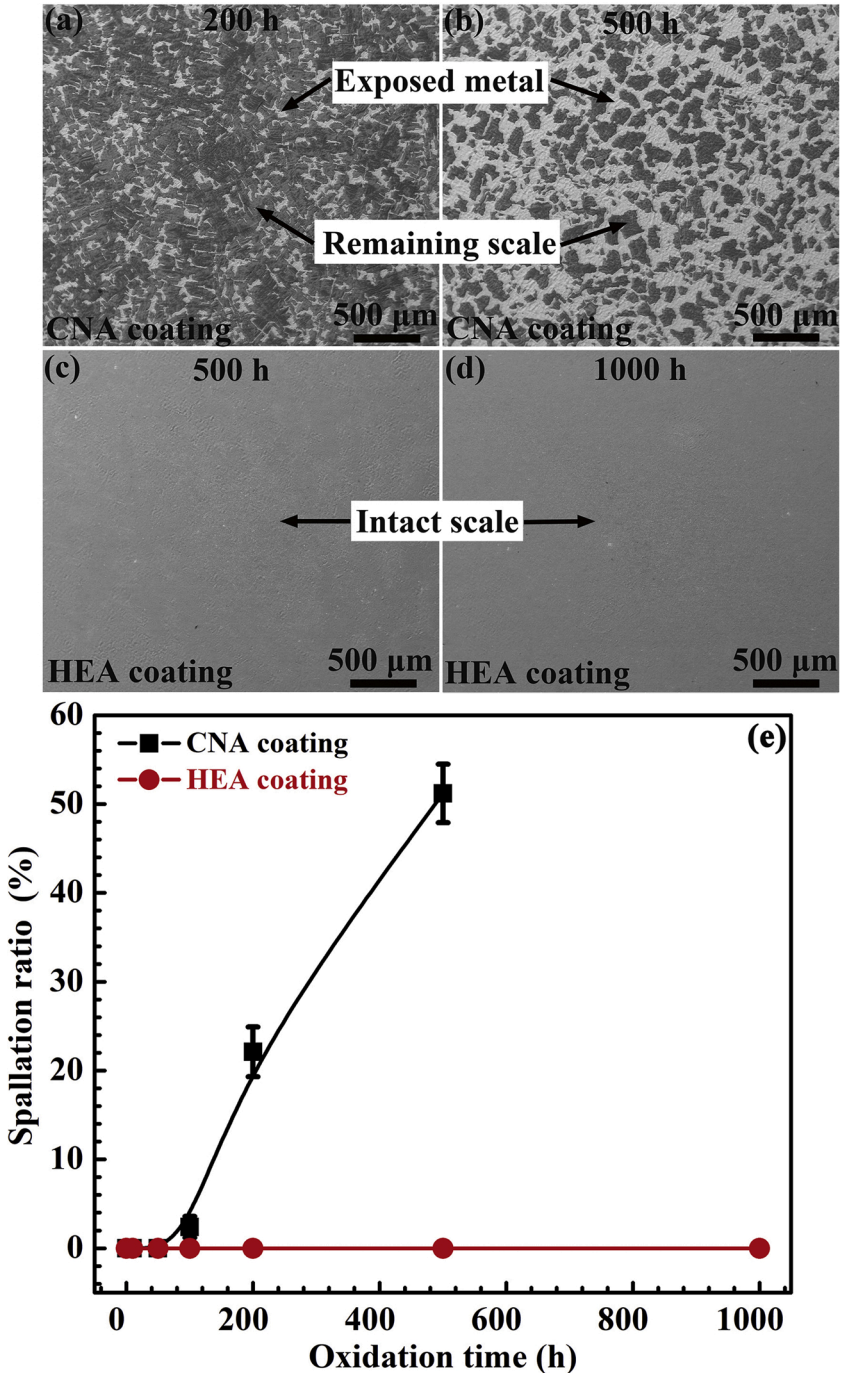

Fig. 4. Spallation degree of oxide scale formed on the two types of coatings at 1100 °C: (a, b) low magnification BSE images, giving an overview of the spalled surface for the CNA coating after 200 h and 500 h oxidation, respectively; (c, d) low magnification BSE images, showing the completely intact oxide scale with the substrate for the HEA coating after 500 h and 1000 h oxidation, respectively; (e) spallation ratio of oxide scale for the two types of coating as a function of the oxidation time (The spallation ratio is defined by the ratio of the area of exposed metal to the area of whole surface. Five BSE images with a magnification of 500×are employed to obtain the average value and the error bar is standard deviation).

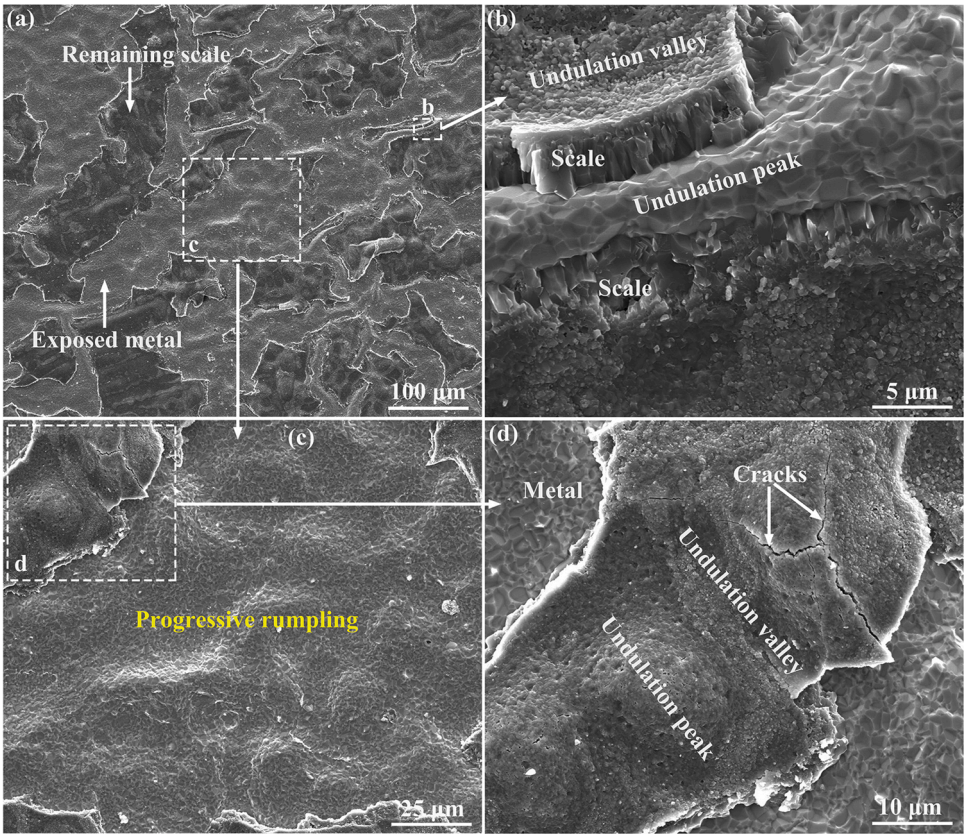

Fig. 5. Surface morphology of the oxide scale formed on the CNA coating after 500 h oxidation at 1100 °C: (a) low magnification SEM image, giving an overview of the spalled surface; (b, c) amplifying SEM images over the region within the white rectangle in (a), showing the spalled interface in detail; (d) amplifying SEM images over the region within the white rectangle in (c), showing the fractured oxide scale.

rate is 100 °C/min and the time cooling to room temperature is about 30 min. The chemical composition of nickel-based Hastelloy® X polycrystalline superalloy can be seen in our previous works [20,26].

2.2. Isothermal oxidation

The as-sintered coating samples were cut into 10 × 10 × 5 mm^3 rectangle plates using a precision cut-off machine (Accutom 5, Struers) equipped with a SiC abrasive cutting blade. All the coatings were ground to the thickness of about 200 μm with SiC abrasive papers and then were polished using 0.05 μm colloidal alumina following standard metallographic approaches. The samples were thoroughly cleaned ultrasonically with acetone prior to oxidation. The isothermal oxidation was carried out at 1100 ℃ in a chamber furnace at atmosphere environment. The samples were placed in the center of chamber furnace near the thermocouple. The oxidized samples were removed from furnace after a required exposure time, and then air-cooled to room temperature outside the furnace in approximately 20 min.

2.3. Samples characterization

The phase constitutions of CNA coating and HEA coating before and after oxidation and oxide scale were determined by X-ray diffraction (XRD, Ultimo IV, Riau, Japan) at 30 kV with Cu Kα radiation. The spectra were collected in a 2θ range of 20~80° with a step size of 0.02° and a scanning speed of 5°/min. The residual stress was measured using photoluminescence piezospectroscopy (PLPS) on a confocal Raman microprobe (LabRAM HR, Horiba Jobin Yvon, France) with a 532 nm Nd:YAG laser. All PLPS spectra were fitted by Labspec software 6.0 with an automatic fitting function using the mixed Gaussian-Lorentzian function. The surface roughness of the oxide scale was measured using an optical profilometer (Zegage™, Zygo, USA). The measurements were conducted using a × 10 lens (Nikon Corporation) and the scanning area was 800 × 800 $μm^2$. The surface and cross-sectional morphology of all samples before and after oxidation was characterized by scanning electron microscopy (SEM, Mira3, Tescan). Additionally, the chemical composition of oxide scale and coatings was identified using energy dispersive X-ray spectroscopy (EDS, Oxford Instruments). Thin lamellae with a thickness less than 50 nm from the as-sintered HEA coating was prepared using a focused ion beam (FIB, GAIA3, Tescan, Czech Republic) and were subsequently analyzed using a scanning transmission electron microscope (STEM, TALOS F200X, FEI, USA) equipped with an energy dispersive X-ray spectroscopy (EDS, XIS Ultra DLD, Kratos, Japan) system.

3. Results

3.1. Microstructures of coatings

Fig. 1 shows the cross-sectional and surface morphology of CNA coating and HEA coating. Two types of coatings adhere well to the substrate through inter-diffusion, which can be indicated by the inter-diffusion zone (IDZ) between the coating and substrate (Fig. 1a, a1, d and d1). The effect of IDZ from the sintering process on the oxidation behavior of two types of coatings can be neglected due to the much higher thicknesses of coatings (200 ± 20 μm) than those of IDZ (about 8 μm for the CNA coating and about 10 μm for the HEA coating). Additionally, these two coatings are both fully dense without occurrence of pores or internal oxide inclusions, which can be attributed to the fast sintering capacity of SPS under vacuum [31].

For the CNA coating, a typical two-phase structure consisting of face-centered cubic (FCC) γ phase (bright contrast) and ordered body-

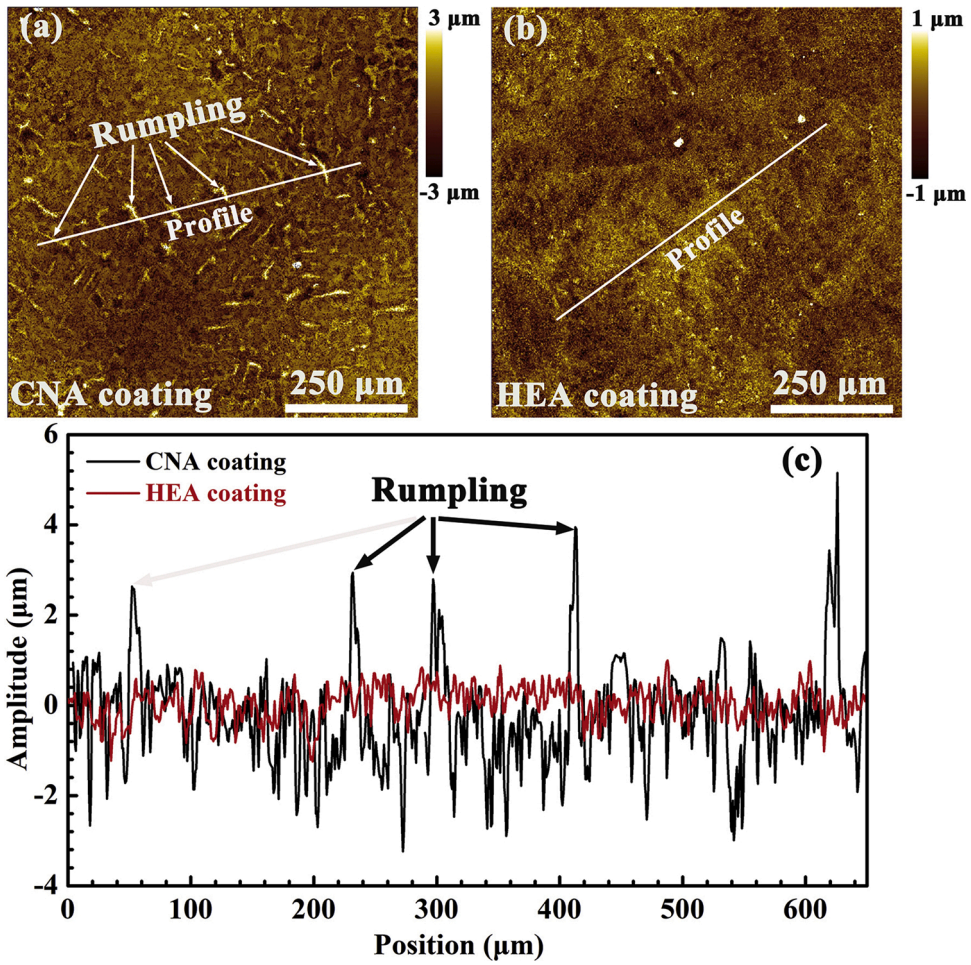

Fig. 6. Profilometer images of two types of coatings after 100 h oxidation at 1100 °C: (a) CNA coating; (b) HEA coating; (c) height profiles of the white lines in (a) and (b).

centered cubic (B2) β phase (dark contrast) can be observed (Fig. 1b and c), which agrees well with the XRD results in Fig. 2. The volume fractions of γ and β phases in the CNA coating are about 64.7 % and 35.3 % respectively, which is measured using Image J software. For the HEA coating, a characteristic two-phase nanostructure composed of disordered body-centered cubic (A2) phase (bright contrast) and β phase (dark contrast) can be clearly seen in combination with the XRD results in Fig. 2. The volume fractions of A2 and β phases are 44.9 % and 55.1 % in the HEA coating.

TEM analysis of HEA coating is also utilized to examine the size and composition of A2 and β phases, which is presented in Fig. 3. It can be clearly seen that A2 phase is enriched with Fe and Cr and β phase is enriched with Ni and Al, while Co is uniformly distributed in the HEA coating. In our recent work [22], the structure of as-cast AlCoCrFeNi alloy has been characterized in detail. The phase constitutions of the HEA coating are same as that of as-cast AlCoCrFeNi alloy, while the phase size in HEA coating (about 500 nm in width) is about five times higher than that (about 100 nm in width) in as-cast AlCoCrFeNi alloy due to sintering [22].

3.2. Spallation resistance of oxide scale

Fig. 4 shows the spallation degree of oxide scale formed on the two types of coatings at 1100 °C as a function of oxidation time. The CNA coating undergoes a severe spallation of oxide scale with a spallation ratio of over 20 % after 200 h oxidation (The bright regions represent the exposed metal surface due to the oxide scale spallation) (Fig. 4a and e). When the oxidation time increases to 500 h for the CNA coating, the oxide scale bears destructive spallation and the spallation ratio exceeds 50 % (Fig. 4b and e). For the HEA coating, the oxide scale is still well adherent with the substrate after 500 h oxidation and no oxide scale spallation can be seen even after 1000 h oxidation (Fig. 4c and d). Based on the results above, the HEA coating exhibits much stronger resistance to oxide scale spallation in comparison to the CNA coating at 1100 °C.

3.3. Oxide scale microstructure

Fig. 5 shows the surface morphology of oxide scale formed on the CNA coating after 500 h oxidation at 1100 °C. It can be clearly seen in Fig. 5a and b that the oxide scale detaches and spalls from the scale/metal interface based on the exposed metal substrate. The progressive surface/interface roughening (also termed as rumpling) develops after 500 h oxidation (Fig. 5c and d). Similar rumpling phenomenon of the NiCoCrAlY coating is also observed and investigated in the previous studies [35,36]. According to the results presented in Fig. 5b and d, the fracture and detachment of oxide scale occur first in these locations of undulation peaks. In other words, the spallation of oxide scale formed on the CNA coating is closely related to the interface rumpling, which will be discussed in later section.

Since the oxide scale undergoes severe spallation after 200 h oxidation for the CNA coating (Fig. 4e), the magnitude of surface roughening of oxide scale for two types of coatings is compared based on the surface morphology of oxide scale after 100 h oxidation. Fig. 6 shows the profilometer images of two types of coatings after 100 h

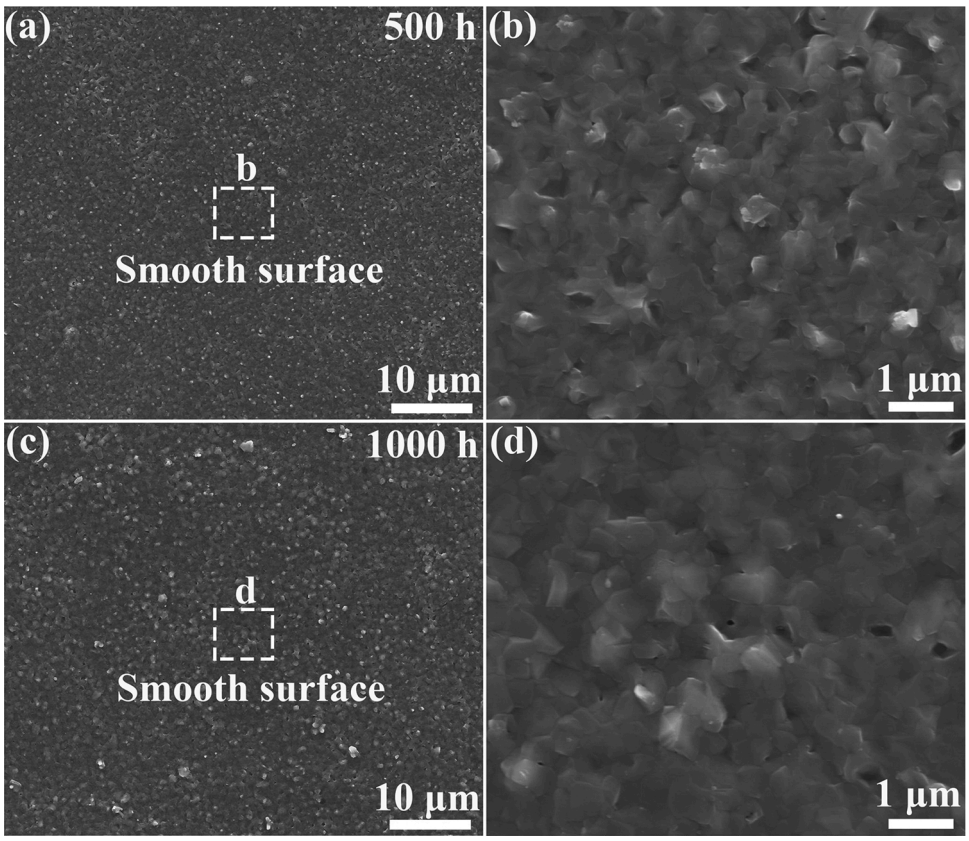

Fig. 7. Surface morphology of oxide scale formed on the two types of coatings at 1100 °C: (a, c) low magnification SEM images and (b, d) amplifying SEM images over the region within the white rectangle in (a) and (c), showing the surface morphology of oxide scale formed on the HEA coating after 500 h and 1000 h oxidation, respectively.

oxidation. The surface topographies (Fig. 6a and b) accompanied with the corresponding height profiles of the line segments (Fig. 6c) indicates that the bright regions with a high surface roughness (3−6 μm) are the locations of surface rumpling for the CNA coating. These results are in accordance with the observations in Fig. 5. For the HEA coating, the surface roughness amplitude of oxide scale is much smaller (< 1 μm) and more uniform along the line segment than that of CNA coating (Fig. 6c), which reveals a much smoother surface for a given oxidation time (e.g. 100 h). The smooth surface of oxide scale formed on the HEA coating after 500 h and 1000 h oxidation is also presented in Fig. 7 to further emphasize the negligible rumpling magnitude.

To further reveal the failure mode of oxide scale formed on the HEA coating, Fig. 8 shows the cross-sectional morphology of oxide scale and substrate for the CNA coating after 500 h oxidation at 1100 °C. Two features should be noted in Fig. 8a: first, the rupture and detachment of oxide scale has already occurred, even if the oxide scale does not spall from the metal substrate; second, the scale rumpling relies on the interface rumpling. These results are consistent with the observations for the spalled surface in Fig. 4. As shown in Fig. 8b, the oxide scale is a double-layer structure consisting of a predominant Al_2O_3 inner layer and an outward spinel layer with a low thickness of about 500 nm, while the thickness of oxide scale reaches about 4.8 μm after 500 h oxidation. According to the corresponding elemental maps, the spinel layer contains all base elements, which is thought to be the common (Co, Ni)(Al, Cr)$_2O_4$ oxides [20]. Since Al flux from the underlying metal substrate required to form Al_2O_3 is sufficient due to the presence of Al-rich β phase (Fig. 8a), the formation of spinel originates from the early transitive oxidation stage. XRD results presented in Fig. 9 also indicate that oxide scale formed on the CNA coating and HEA coating mainly consist of Al_2O_3 after 500 h oxidation. The spinel at the top of Al_2O_3 scale for the CNA coating is not detected using XRD, probably due to its low concentration.

To further confirm the strong resistance to oxide scale spallation for the HEA coating after oxidation and compare this with the CNA coating, Fig. 10 shows the cross-sectional morphology of HEA coating after 500 h and 1000 h oxidation at 1100 °C. Three important points should be pointed out here: first, the scale/metal interface is smooth and no obvious interface rumpling can be seen after 500 h and 1000 h oxidation (Fig. 10a and c); second, the HEA coating comprises β and γ phases (Fig. 10a and c), in conjunction with XRD results in Fig. 8; third, a continuous Al-depletion layer from the phase transformation of β to γ due to the growing Al_2O_3 scale forms beneath the Al_2O_3 scale (Fig. 10a and c). Similar Al-depletion layer resulting from the growth of Al_2O_3 scale is also found for the oxidized CNA coating (Fig. 8a). In addition, the thickness of oxide scale 500 h oxidation is about 3.8 μm, which is much lower than that of CNA coating (Fig. 8b and 10b). Even after 1000 h oxidation, the thickness of oxide scale is merely about 4.9 μm, which is basically equal to the scale thickness (about 4.6 μm) formed on the as-cast Y-Hf co-doped AlCoCrFeNi alloy after 1000 h oxidation at 1100 °C [37]. Compared with the oxidized CNA coating, a Cr-containing $(Al,Cr)_2O_3$ layer rather than a spinel layer forms at the top of Al_2O_3 layer combined with the elemental maps (Fig. 10d). Generally, the HEA coating exhibits a much stronger resistance to the scale rumpling and a much slower oxidation rate in comparison to the CNA coating at 1100 °C.

3.4. Oxidation kinetics

The overall thickening of oxide scale formed on two types of coatings is dominated by the growth of an Al_2O_3 scale, which is a diffusion-controlled process. Therefore, the growth of oxide scale should follow a parabolic law according to the classical oxidation theory [38]:

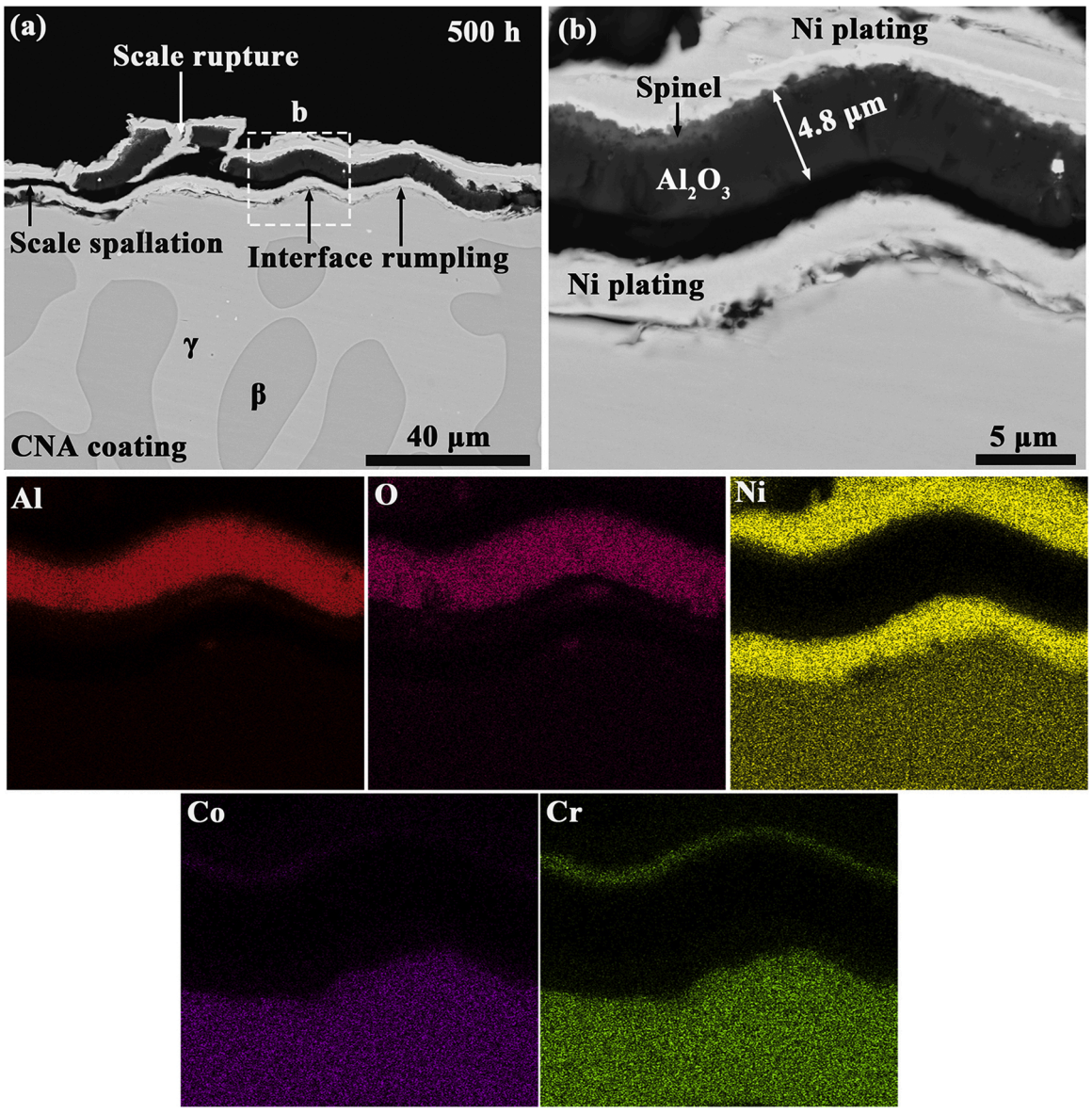

Fig. 8. Cross-sectional morphology of CNA coating after 500 h oxidation at 1100 °C: (a) a low magnification BSE image, showing the structure of oxide scale and substrate; (b) an amplifying BSE image from the region marked by white rectangle in (a) and the corresponding elemental maps, showing the composition of oxide scale and substrate.

$$h^2 = k_p t \quad (1)$$

where k_h, h and t are the oxidation rate constant, the thickness of oxide scale and oxidation time, respectively. For the CNA coating and HEA coating, the oxidation kinetics can be accurately measured by the thickness of oxide scale, especially in the case of the uniform scale thickness and the negligible internal oxidation (Figs. 8 and 10).

Fig. 11 shows the evolution of oxide scale thickness for the two types of coating as a function of oxidation time at 1100 °C. Based on the linear fitting, the oxidation rate constants of CNA coating and HEA coating are calculated to be 2.6×10^{-2} μm^2/h and 1.3×10^{-2} μm^2/h, respectively. In conclusion, the oxidation rate contant of HEA coating at 1100 °C is 50 % lower than that of CNA coating. In our previous work [37], the oxidation rate constant of an as-cast AlCoCrFeNi alloy with same amount of Y and Hf co-doping after 1000 h oxidation at 1100 °C is 1.1×10^{-2} μm^2/h, which is very closed to that for the oxidized HEA coating. In other words, the extremely low oxidation rate for the as-cast Y-Hf co-doped AlCoCrFeNi alloy can be still maintained, even if this alloy is fabricated into a coating material.

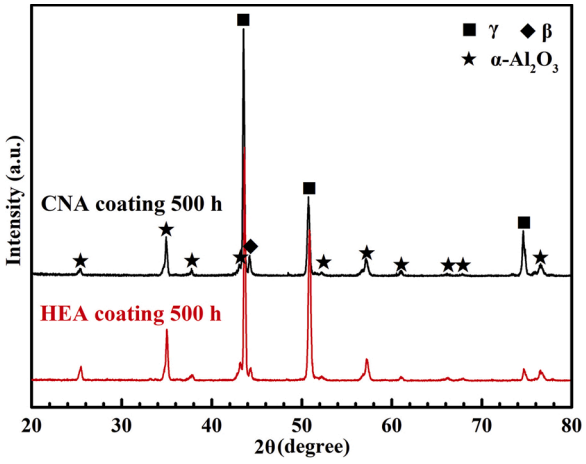

Fig. 9. XRD results of two types of coatings after oxidation for 500 h at 1100 °C.

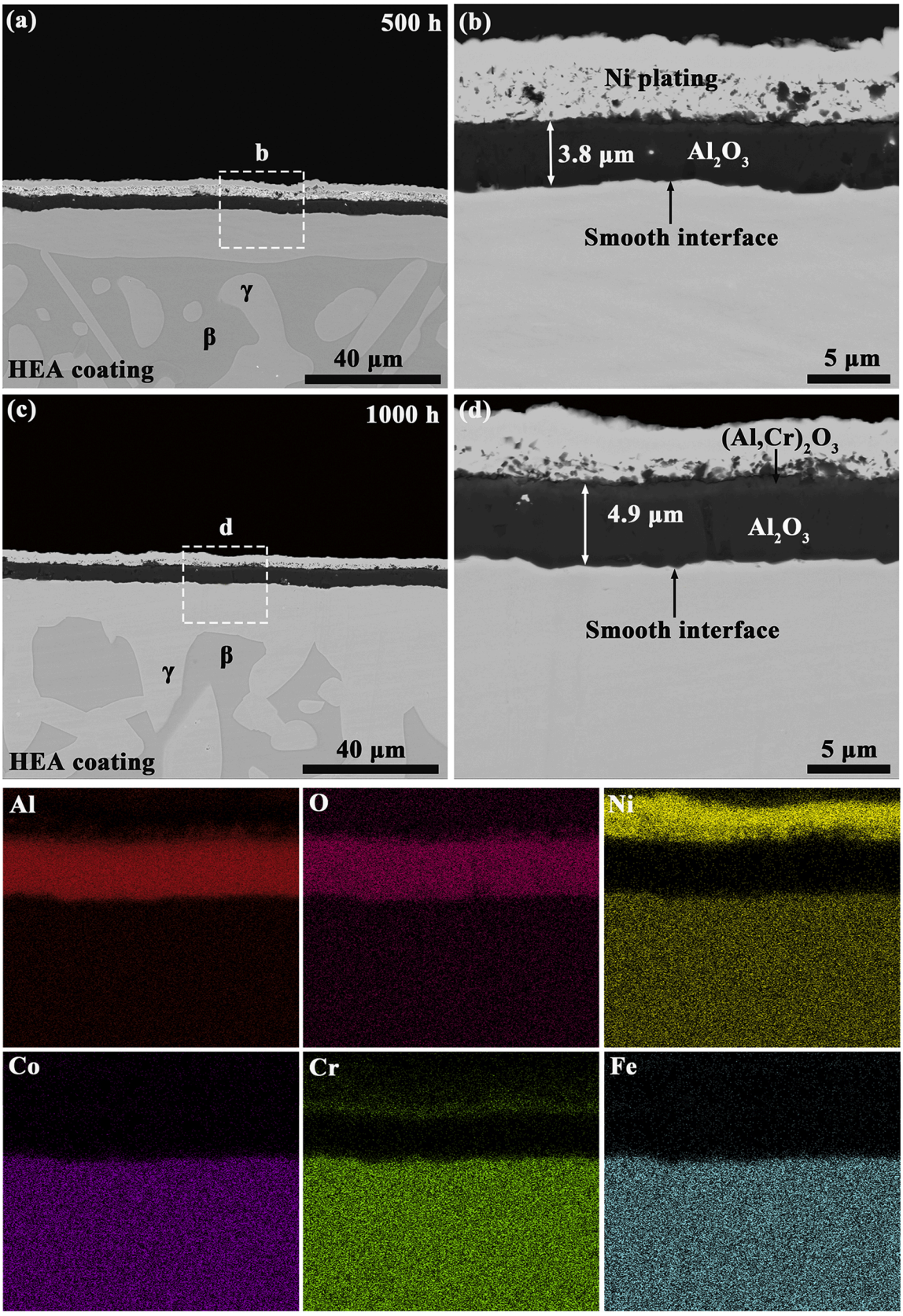

Fig. 10. Cross-sectional morphology of HEA coating after oxidation at 1100 °C: (a, b) low and high magnification BSE images, showing the structure of oxide scale and substrate after 500 h oxidation; (b, c) low and high magnification BSE images, showing the structure of oxide scale and substrate after 1000 h oxidation; The corresponding elemental maps, showing the composition of oxide scale and substrate.

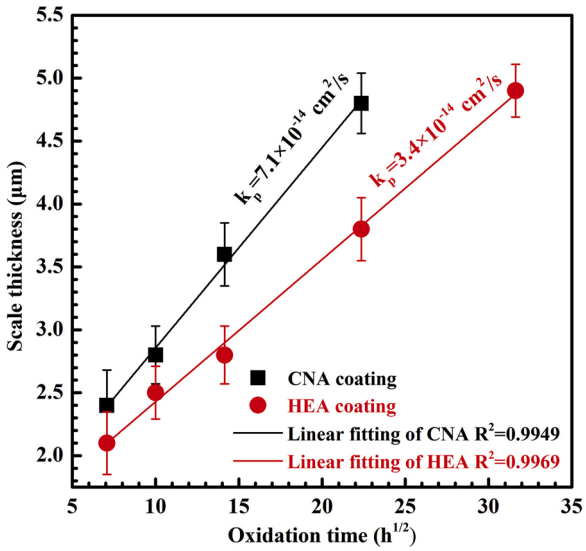

Fig. 11. Evolution of oxide scale thickness for the two types of coatings as a function of the square root of oxidation time at 1100 °C. The thickness of oxide scale formed on the CNA coating was merely measured until 500 h oxidation due to the severe scale spallation.

To directly compare the oxidation rate constant of HEA coating with the typical Al_2O_3 - forming alloys (e.g. NiAlHf and FeCrAlY), the oxidation rate constants based on the oxide scale thickness can be converted into those based on the mass gain by [39,40]:

$$k_m = \left(\frac{3M_O\rho_{Al_2O_3}}{M_{Al_2O_3}}\right)^2 k_h \quad (2)$$

where k_m is the oxidation rate constant based on the mass gain. M_O (16 g/mol) and $M_{Al_2O_3}$ (102 g/mol) are molar mass of O and Al_2O_3, respectively. $\rho_{Al_2O_3}$ (3.98 g/cm^3) is the density of α-Al_2O_3. The oxidation kinetics based on the scale thickness can be accurately converted into that based on the mass gain due to the uniform oxide scale thickness and the absence of internal oxidation. Therefore, the oxidation rate constants based on the mass gain of CNA coating and HEA coating are 2.5×10^{-13} g^2 cm^{-4} s^{-1} and 1.2×10^{-13} g^2 cm^{-4} s^{-1}, respectively. Through comparing the oxidation rate constant of HEA coating (1.2×10^{-13} g^2 cm^{-4} s^{-1}) with those from NiAlHf (1.6×10^{-13} g^2 cm^{-4} s^{-1}) and FeCrAlY (0.98–4.4 $\times 10^{-13}$ g^2 cm^{-4} s^{-1}) reported by Pint et al. [9,10], it can be clearly indicated that the oxidation rate of HEA coating is comparable to those of NiAlHf and FeCrAlY.

Table 2
Columnar grain width in the double-layer oxide scale formed on the CNA coating and HEA coating after 500 h oxidation. (The columnar grain width is obtained by SEM image (with a magnification of 20000×) width divided by the overall numbers of columnar grains in a single SEM image. Five SEM images are employed to measure the average columnar grain width using Image J software and meanwhile the error bar represents the standard deviation of measured widths.).

Samples	Columnar grain width after 500 h oxidation (μm)
CNA coating	1.1 ± 0.2
HEA coating	1.8 ± 0.3

4. Discussion

4.1. Growth mechanism of oxide scale

The oxide scale formed on the CNA coating consists of an inner Al_2O_3 layer and an outward spinel layer with a low thickness of about 500 nm (Fig. 8b). In the early oxidation stage, all base elements of the CNA coating will be oxidized to form spinel. Similar spinel formation at the top of Al_2O_3 layer for a NiCoCrAlY coating is extensively reported in previous works [40–42]. This brittle spinel is detrimental as it reduces the protectiveness of the oxide scale and undermines the interfacial adhesion, especially in the case of YSZ TBCs [41,43]. Once a continuous oxide scale develops at the metal surface, the critical Al concentration required to Al_2O_3 will be significantly lowered due to a much lower oxygen partial pressure at the scale/metal interface than that at the scale surface. Thus the thickening of oxide scale is still dominated by Al_2O_3 growth for the CNA coating (Fig. 8).

However, for the HEA coating, no spinel can be observed at the scale surface, except for the formation a thin Cr-containing $(Al,Cr)_2O_3$ layer at the top of Al_2O_3 layer (Fig. 10). The initially formed Cr_2O_3 interacts with the Al_2O_3 layer forming a solid solution phase $(Al,Cr)_2O_3$, which is also found on the oxidized NiCrAl or NiCoCrAl alloys [44,45]. The inhibition of spinel formation for the HEA coating is attributed to the intrinsic nanostructure of HEA coating (Fig. 1e and f). According the selective oxidation theory of Al_2O_3, the nanostructure provides a large amount of phase boundaries, which can significantly increase the outward Al diffusion paths and thus accelerates Al flux reaching coating surface to form Al_2O_3 [41,46]. Eventually, the formation of spinel is well inhibited. It should be mentioned that the Al content in the HEA coating (10.7 wt %) is lower than that in the CNA coating (12.3 wt%). In theory, a higher Al concentration in the substrate should be more preferential Al_2O_3 formation, but the formation of spinel occurs for the CNA coating. Two factors might contribute to the absence of spinel for the HEA coating. First, the Al activity could be is higher in the AlCoCrFeNi matrix, thus leading to preferential Al_2O_3 formation. Second, as mentioned

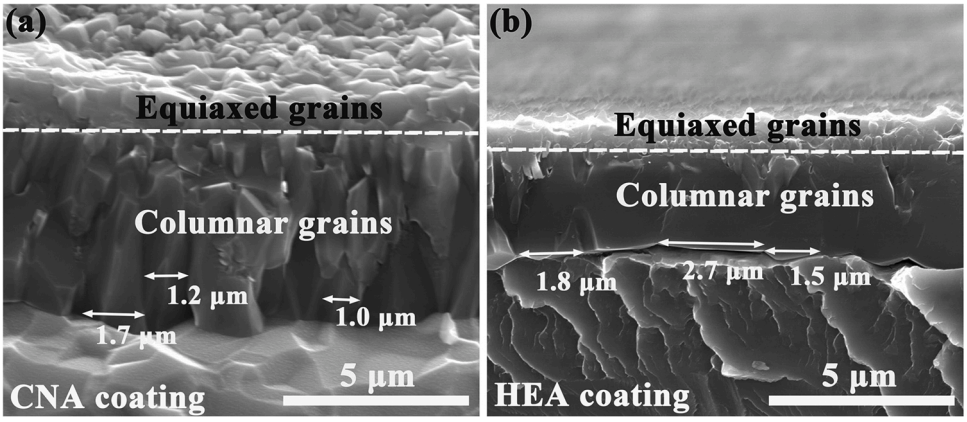

Fig. 12. Fractural structure of oxide scale formed on the two coatings after 500 h oxidation at 1100 °C: (a) CNA coating; (b) HEA coating.

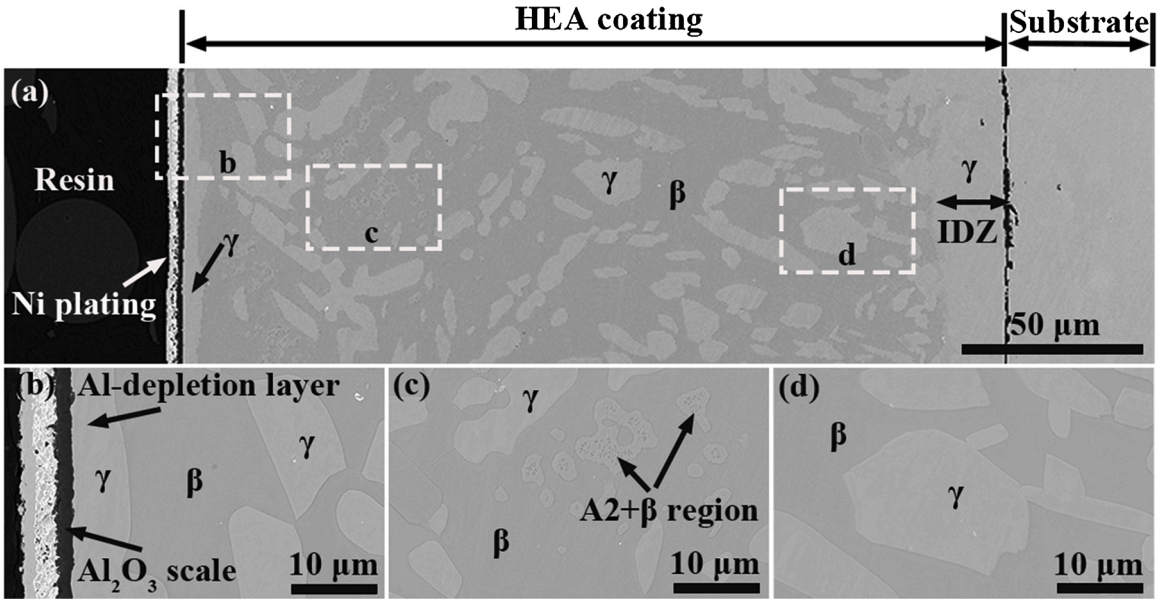

Fig. 13. Cross-sectional morphology of HEA coating after 50 h oxidation 1100 °C: (a) a low magnification BSE image, giving an overview of coating and substrate; (b, c and d) enlarged views of the designated areas in (a), showing the phase constitutions in different areas of HEA coating.

previously, the nanostructure with a high phase boundary density could facilitate the formation of Al_2O_3.

Since the formation of thin spinel or $(Al,Cr)_2O_3$ layer at the top of Al_2O_3 layer derives from the early transitive oxidation stage, the overall thickening of oxide scale during the prolonged oxidation is still controlled by the growth of Al_2O_3 for the two coatings (Figs. 8 and 10). To understand the growth mechanism of Al_2O_3 layer during the prolonged oxidation, the fractural structure of oxide scale formed on the two coatings is presented in Fig. 12. First, a typical double-layer scale structure composed of the outward equiaxed grains and the inward columnar grains in contact with the metal substrate suggests concurrent diffusion of Al and O (Fig. 12a and b) [47]. Second, the predominant columnar grain structure in the scale indicates that the growth of Al_2O_3 scale is dominated by the inward O diffusion [48,49]. A predominant columnar grain structure of scale is usually observed on the reactive elements (RE) doped NiAl, FeCrAl, NiCoCrAl alloys [13,47,50]. The dynamical segregation of RE (Y and Hf) ions from scale/metal interface to scale surface along Al_2O_3 scale grain boundaries can effectively block the outward Al diffusion, and thus the inward O diffusion is predominant growth mechanism of Al_2O_3 scale [51].

Since the thickening of oxide scale formed on the two coatings during prolonged oxidation is controlled by the growth of Al_2O_3 scale with a predominant columnar grain structure, the columnar grain boundaries of Al_2O_3 scale are fast paths of inward O diffusion. A lower columnar grain width signifies a higher grain boundary density, thus a higher amount of inward O diffusion paths. It can be clearly found in Fig. 12 that the columnar grain width of Al_2O_3 scale for the HEA coating is much higher than that for the CNA coating. In addition, the average columnar grain width based on the fractural surface of oxide scale formed on the two coatings after 500 h oxidation is presented in Table 2. The average columnar grain width for the HEA coating (1.8 ± 0.3 μm) is 64 % higher than that of CNA coating (1.1 ± 0.2 μm). Therefore, the fast paths of inward O diffusion in the Al_2O_3 scale for the HEA coating is much lower than those for the CNA coating, thus contributing to a much lower oxidation rate. It is possible that the unique structure and chemical composition of HEA coating induces the formation of coarse columnar grains, but the formation mechanism of coarse columnar grains is still unclear and more works are required to understand this point.

4.2. *Interface rumpling and failure mechanism of oxide scale*

It is clearly indicated that the CNA coating shows obvious scale/metal interface rumpling, while the interface rumpling is well inhibited for the HEA coating (Figs. 5–9). It is reported that the interface rumpling initiates cracks nucleation and propagation, and thus leads to the scale failure [35,36,52,53]. For the CNA coating, the inter-diffusion between coating and substrate at high temperatures causes the phase transformation of β to γ, which involves a volume shrinkage up to 38 % [54]. Since the volume change is constrained by the substrate, a stress will be generated in the CNA coating at high temperatures. The high temperature stress can facilitate the coating creep through activating the grain sliding, thus inducing the interface rumpling [36].

For the HEA coating, the original structure consists of A2 and β phases (Figs. 1–3), but the coating structure is dominated by the γ and β phases after oxidation due to the growth of oxide scale and the inter-diffusion with substrate (Figs. 9 and 10). Fig. 13 shows the overall cross-section of HEA coating after 50 h oxidation 1100 °C. It can be clearly seen that the HEA coating predominantly comprises γ phase (about 48.5 %) and β phase (about 50.4 %) and only minor amount of A2 phase (about 1.1 %) is preserved after 50 h oxidation (Fig. 13b–d). In our recent work [37], an extremely low amount of γ phase merely precipitates from the grain boundary in the as-cast AlCoCrFeNi alloy after 1000 h oxidation at 1100 °C. Thus, the formation of a large amount of γ phase in the HEA coating primarily derives from the inter-diffusion of coating with substrate, rather than the growth of oxide scale.

Since the γ and β phases is primary phase constitutions in the HEA coating after 50 h oxidation, the volume change of HEA coating during the prolonged oxidation is determined by phase transformation of β to γ. Fig. 14 shows the IDZ thickness after 500 h oxidation at 1100 °C and the evolution of volume fraction of γ and β phases with the increasing oxidation time at 1100 °C for two coatings. As presented in Fig. 14a and b, the IDZ thicknesses for two coatings is almost equal (about 100 μm) after 500 h oxidation, suggesting a similar inter-diffusion level. In addition, the total amount of β to γ phase transformation is also comparable after oxidation from 50 h to 500 h for two coatings (Fig. 14c and d). Therefore, the volume change caused by β to γ transformation should be substantially equal for two coatings, which leads to a comparable high temperature stress level. However, the interface rumpling is well suppressed for the HEA coating.

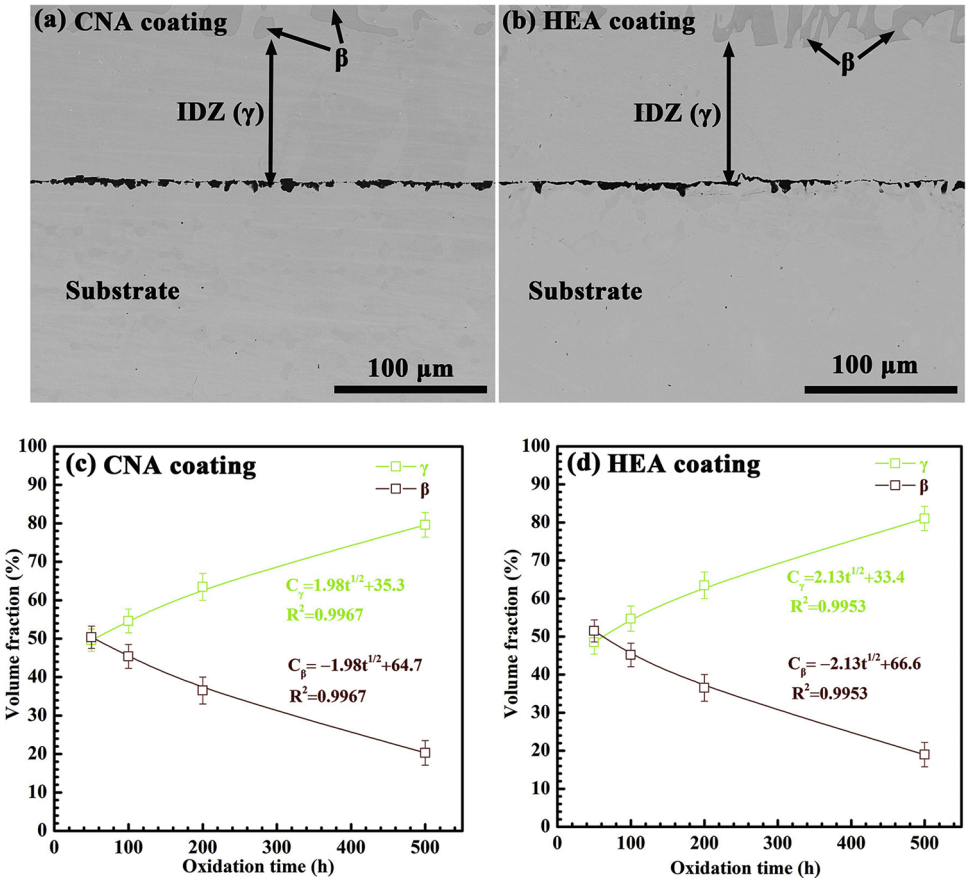

Fig. 14. Low magnification BSE images, showing the thickness of IDZ for the CNA coating (a) and the HEA coating (b) after 500 h oxidation at 1100 °C. Evolution of volume fraction of γ and β phases as a function of oxidation time for the CNA coating (c) and the HEA coating (d).

Thus, it is proposed that the HEA coating might have a stronger creep resistance in comparison to the CNA coating. At such a high temperature (1100 °C), the creep of coating is actually controlled by atomic diffusion [36]. Sluggish diffusion effect of compositional elements in the high-entropy materials is very important, which can lead to exceptional high-temperature creep resistance and impressive high-temperature strength [55–57]. It is proposed by Yeh et.al that sluggish diffusion effect derives from the fluctuation in lattice potential energy (LPE) [57]. The distorted multi-principal element lattice in the HEA contributes to fluctuated LPE for the migration of an atom from one site to another because each site is surrounded by different kinds of atoms and thereby causes different total interaction energy [57,58]. As a result, this fluctuated LPE in the HEA would lead to the more difficult diffusion of atoms than that in the lattice with uniform LPE. Sluggish diffusion effect for Al, Cr and Fe is also observed in the FCC AlCoCrFeNi HEA [59].

Even if the HEA coating is a two-phase structure, the configurational entropy (ΔS_{conf}) of each phase (γ and β) in the HEA coating after 500 h oxidation at 1100 °C can be still calculated by [60]:

$$\Delta S_{conf} = -RX_i \ln(X_i) \tag{3}$$

where X_i is the atom fraction of element i and R is the gas constant. The atom fraction of each element based on the SEM-EDS point analysis is presented in Table 3. Therefore, the configurational entropy of γ and β are respectively 1.56R and 1.51R, which are higher than the present classification of high entropy alloys (>1.5R) [60]. In other words, the γ and β in the HEA coating after prolonged oxidation at 1100 °C can be regarded as a high-entropy alloy, respectively. Based on the analysis mentioned above, it is speculated that the sluggish diffusion effect of each phase in the HEA coating can increase the creep resistance by lowering the rate of atomic diffusion and thereby suppress the interface rumpling.

It is well accepted that the detachment of oxide scale from the scale/metal interface is predominantly driven by the elastic strain energy stored in the attached scale G, resulting from the constantly thickening scale and the residual stress in scale. The detachment of oxide scale will occur, once G exceeds the interfacial toughness G_c [8]:

$$G = \frac{(1-\nu_{ox}^2)\sigma^2 h_{ox}}{2E_{ox}} \tag{4}$$

where E_{ox}, h_{ox} and ν_{ox} are Young' modulus, thickness and Poisson' ratio of oxide scale, respectively. The residual stress in oxide scale σ can be determined at room temperature, using PLPS technique, by [13,61]

$$\Delta v = 5.07\sigma \tag{5}$$

where Δv is the peak shift from R2 line of Al_2O_3, which is obtained using a stress-free sapphire as the stress reference. The residual stress in oxide scale originates predominantly from the thermal expansion mismatch between the scale and metal substrate and the growth of oxide scale [7].

Fig. 15 shows the evolution of residual stress in the oxide scale formed on the two coatings with the increasing oxidation time at 1100 °C. Two coatings show no obvious difference in stress level and stress evolution during the prolonged oxidation. The slight increase in stress level before 10 h oxidation probably results from the gradually continuous growth of oxide scale [62]. Eventually, the residual stress reaches a stable stress level in a compressively stressed state (about -4.8 GPa). Based on the Eq. (4), the stored elastic strain energy in the oxide scale for two coatings is determined by the oxide scale thickness because of the substantially equal residual stress. Therefore, a higher oxide scale thickness for the CNA coating contributes to a higher elastic

Table 3
Chemical composition of γ and β phases in the HEA coating after 500 h oxidation at 1100 °C based on the SEM-EDS point analysis.

Phases	Elements (at. %)				
	Al	Co	Cr	Fe	Ni
γ	8.9 ± 0.1	23.4 ± 0.2	23.8 ± 0.2	25.7 ± 0.3	18.3 ± 0.2
β	30.3 ± 0.2	17.1 ± 0.2	9.9 ± 0.1	12.2 ± 0.2	30.5 ± 0.3

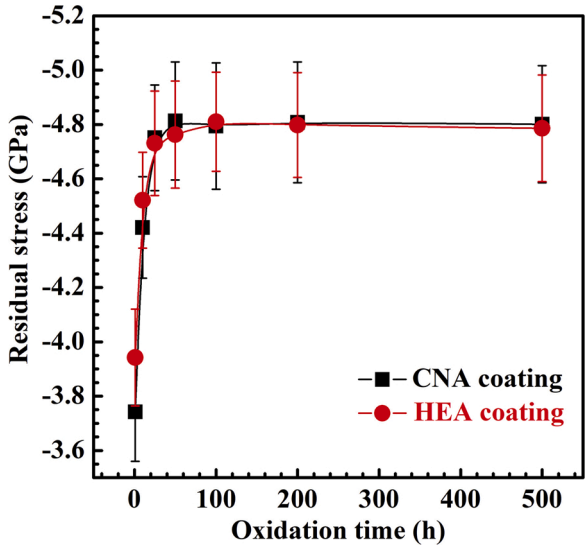

Fig. 15. Evolution of residual stress in the oxide scale formed on the two coatings as a function of the oxidation time at 1100 °C.

strain energy in the oxide scale, thus a higher driving force for the scale spallation. As shown in Fig. 5, the spallation of oxide scale for the CNA coating occurs along the scale/metal interface. In addition, no interfacial imperfections (e.g. pores or oxide intrusions) can be found at the spalled interface (Fig. 5a and c) [13]. Thus, the nucleation of interface cracks is merely initiated through the interface rumpling (Fig. 8a and b). The interface rumpling develops a tensile stress around the undulation peaks across the scale/metal interface, where the oxide scale is in a compressively stressed state in the lateral direction (Fig. 5b and d). The tensile stress leads to the interfacial cracking easily [7]. Meanwhile, for the CNA coating, a higher driving force for the scale spallation will accelerate the propagation of interface cracks. Once the length of interface cracks reaches the critical size of oxide scale spallation, the oxide scale will spall off along the interface. For the HEA coating, both the inhibition of interface rumpling and a lower driving force for the scale spallation contribute to a stronger resistance to the scale spallation.

5. Conclusions

In this study, a highly oxidation and spallation resistant AlCoCrFeNi high-entropy alloy coating (HEA coating) with Y-Hf co-doping is reported. Additionally, its oxidation behavior is systematically investigated at 1100 °C and compared with that of the conventional NiCoCrAl alloy coating (CNA coating) with same Y-Hf co-doping. The following conclusions can be drawn.

(1) The HEA coating consists of nanostructured A2 (disordered BCC) and β (B2, ordered BCC) phases, which can facilitate the formation of Al_2O_3 and thus inhibit the formation of spinel in the early oxidation stage. After the prolonged oxidation, the HEA coating transforms into the two-phase structure of γ and β, which is predominantly attributed to the inter-diffusion of coating with the substrate.
(2) The HEA coating exhibits an extremely low oxidation rate with an oxidation rate constant of 1.3×10^{-2} μm^2/h at 1100 °C, which is 50 % lower than that (2.6×10^{-2} μm^2/h) of the CNA coating. The low oxidation rate for the HEA coating is attributed to the much higher width of columnar grains in the Al_2O_3 scale in comparison to that for the CNA coating.
(3) The scale/metal interface rumpling is well suppressed for the HEA coating. It is proposed that the elimination of interface rumpling is likely to result from the higher creep resistance of HEA coating, originating from the unique sluggish diffusion effect in a high-entropy alloy.
(4) The HEA coating shows superior resistance to the oxidation resistance compared with that of the CNA coating. Almost no spallation of oxide scale can be observed after 1000 h oxidation at 1100 °C.

In summary, both the extremely low oxidation rate and the strong inhibition of interface rumpling for the HEA coating contribute to its superior resistance to scale spallation, which makes it a good candidate material for the bond coat in TBCs or the oxidation protective coating at high temperatures.

Data availability

The raw/processed data required to reproduce these findings can be shared upon reasonable requests.

CRediT authorship contribution statement

Jie Lu: Conceptualization, Data curation, Writing - original draft, Writing - review & editing. **Han Zhang:** Writing - review & editing. **Ling Li:** Writing - review & editing. **Ying Chen:** Investigation, Methodology. **Xuanzhen Liu:** Investigation, Methodology. **Xiaofeng Zhao:** Fouding acquisition, Conceptualization, Writing - review & editing. **Fangwei Guo:** Methodology, Formal analysis. **Ping Xiao:** Methodology, Formal analysis.

Declaration of Competing Interest

The authors declare that they have no known competing financial interests or personal relationships that could have appeared to influence the work reported in this paper.

Acknowledgement

This work was financially supported by National Natural Science Foundation of China (51971139) and National Major Science and Technology Project of China (2017-VI-0011-0083)

References

[1] M.J. Pomeroy, Coatings for gas turbine materials and long term stability issues, Mater. Des. 26 (2005) 223–231.
[2] D.R. Clarke, M. Oechsner, N.P. Padture, Thermal-barrier coatings for more efficient gas-turbine engines, MRS Bull. 37 (2012) 891–898.
[3] N.P. Padture, M. Gell, E.H. Jordan, Thermal barrier coatings for gas-turbine engine applications, Science 296 (2002) 280–284.
[4] J.T. DeMasi-Marcin, D.K. Gupta, Protective coatings in the gas turbine engine, Surf. Coat. Technol. 68-69 (1994) 1–9.
[5] D. Naumenko, V. Shemet, L. Singheiser, W.J. Quadakkers, Failure mechanisms of thermal barrier coatings on MCrAlY-type bondcoats associated with the formation of the thermally grown oxide, J. Mater. Sci. 44 (2009) 1687–1703.
[6] T.J. Nijdam, W.G. Sloof, Effect of reactive element oxide inclusions on the growth kinetics of protective oxide scales, Acta Mater. 55 (2007) 5980–5987.
[7] A.G. Evans, D.R. Mumm, J.W. Hutchinson, G.H. Meier, F.S. Pettit, Mechanisms controlling the durability of thermal barrier coatings, Prog. Mater. Sci. 46 (2001) 505–553.

[8] J.W. Hutchinson, M.Y. He, A.G. Evans, The influence of imperfections on the nucleation and propagation of buckling driven delaminations, J. Mech. Phys. Solids 48 (2000) 709–734.
[9] B.A. Pint, Optimization of reactive-element additions to improve oxidation performance of alumina-forming alloys, J. Am. Ceram. Soc. 86 (2003) 686–695.
[10] B.A. Pint, K.L. More, I.G. Wright, Effect of quaternary additions on the oxidation behavior of Hf-Doped NiAl, Oxid. Met. 59 (2003) 257–283.
[11] H. Peng, H. Guo, J. He, S. Gong, Microscale lamellar NiCoCrAlY coating with improved oxidation resistance, Surf. Coat. Technol. 207 (2012) 110–116.
[12] E. Hejrani, D. Sebold, W.J. Nowak, G. Mauer, D. Naumenko, R. Vaßen, W. J. Quadakkers, Isothermal and cyclic oxidation behavior of free standing MCrAlY coatings manufactured by high-velocity atmospheric plasma spraying, Surf. Coat. Technol. 313 (2017) 191–201.
[13] J. Lu, Y. Chen, C. Zhao, H. Zhang, L. Luo, B. Xu, X. Zhao, F. Guo, P. Xiao, Significantly improving the oxidation and spallation resistance of a MCrAlY alloy by controlling the distribution of yttrium, Corros. Sci. 153 (2019) 178–190.
[14] H. Yao, Z. Bao, M. Shen, S. Zhu, F. Wang, A magnetron sputtered microcrystalline β-NiAl coating for SC superalloys. Part II. Effects of a NiCrO diffusion barrier on oxidation behavior at 1100 °C, Appl. Surf. Sci. 407 (2017) 485–494.
[15] N. Birks, G.H. Meier, F.S. Pettit, Introduction to the High Temperature Oxidation of Metals, second edition, 2006.
[16] G.W. Goward, Progress in coatings for gas turbine airfoils, Surf. Coat. Technol. 108-109 (1998) 73–79.
[17] K.G. Field, S.A. Briggs, K. Sridharan, R.H. Howard, Y. Yamamoto, Mechanical properties of neutron-irradiated model and commercial FeCrAl alloys, J. Nucl. Phys. Mater. Sci. Radiat. Appl. 489 (2017) 118–128.
[18] Y. Yamamoto, B.A. Pint, K.A. Terrani, K.G. Field, Y. Yang, L.L. Snead, Development and property evaluation of nuclear grade wrought FeCrAl fuel cladding for light water reactors, J. Nucl. Phys. Mater. Sci. Radiat. Appl. 467 (2015) 703–716.
[19] M.J. Lance, K.A. Unocic, J.A. Haynes, B.A. Pint, APS TBC performance on directionally-solidified superalloy substrates with HVOF NiCoCrAlYHfSi bond coatings, Surf. Coat. Technol. 284 (2015) 9–13.
[20] J. Lu, H. Zhang, Y. Chen, X. Zhao, F. Guo, P. Xiao, Effect of microstructure of a NiCoCrAlY coating fabricated by high-velocity air fuel on the isothermal oxidation, Corros. Sci. 159 (2019) 108126.
[21] Z. Shen, L. He, Z. Xu, R. Mu, G. Huang, Morphological evolution and failure of LZC/YSZ DCL TBCs by electron beam-physical vapor deposition, Materialia 4 (2018) 340–347.
[22] J. Lu, Y. Chen, H. Zhang, L. Li, L. Fu, X. Zhao, F. Guo, P. Xiao, Effect of Al content on the oxidation behavior of Y/Hf-doped AlCoCrFeNi high-entropy alloy, Corros. Sci. 170 (2020) 108691.
[23] K.R. Lim, K.S. Lee, J.S. Lee, J.Y. Kim, H.J. Chang, Y.S. Na, Dual-phase high-entropy alloys for high-temperature structural applications, J. Alloys. Compd. 728 (2017) 1235–1238.
[24] H.X. Zhu, N.A. Fleck, A.C.F. Cocks, A.G. Evans, Numerical simulations of crack formation from pegs in thermal barrier systems with NiCoCrAlY bond coats, Mater. Sci. Eng. A. 404 (2005) 26–32.
[25] H. Yao, L. Yang, Z. Bao, S. Zhu, F. Wang, Low inter-diffusivity γ'-base bondcoats for single crystal superalloy René N5. II: cyclic oxidation behavior at 1100 °C, Corros. Sci. 159 (2019) 108127.
[26] L. Luo, X. Shan, Z. Zou, C. Zhao, X. Wang, A. Zhang, X. Zhao, F. Guo, P. Xiao, A high performance NiCoCrAlY bond coat manufactured using laser powder deposition, Corros. Sci. 126 (2017) 356–365.
[27] A.H. Pakseresht, A.H. Javadi, M. Bahrami, F. Khodabakhshi, A. Simchi, Spark plasma sintering of a multilayer thermal barrier coating on Inconel 738 superalloy: microstructural development and hot corrosion behavior, Ceram. Int. 42 (2016) 2770–2779.
[28] P. Audigié, S. Selezneff, A. Rouaix-Vande Put, C. Estournès, S. Hamadi, D. Monceau, Cyclic oxidation behavior of TBC systems with a Pt-Rich γ-Ni+γ′-Ni3Al bond-coating made by SPS, Oxid. Met. 81 (2013) 33–45.
[29] D. Monceau, D. Oquab, C. Estournes, M. Boidot, S. Selezneff, Y. Thebault, Y. Cadoret, Pt-modified Ni aluminides, MCrAlY-base multilayer coatings and TBC systems fabricated by spark plasma sintering for the protection of Ni-base superalloys, Surf. Coat. Technol. 204 (2009) 771–778.
[30] J. Song, K. Ma, L. Zhang, J.M. Schoenung, Simultaneous synthesis by spark plasma sintering of a thermal barrier coating system with a NiCrAlY bond coat, Surf. Coat. Technol. 205 (2010) 1241–1244.
[31] F. Nozahic, C. Estournès, A.L. Carabat, W.G. Sloof, S. van der Zwaag, D. Monceau, Self-healing thermal barrier coating systems fabricated by spark plasma sintering, Mater. Des. 143 (2018) 204–213.
[32] J. Lu, Y. Chen, H. Zhang, C. Zhao, X. Zhao, F. Guo, P. Xiao, Superior oxidation and spallation resistant NiCoCrAlY bond coat via homogenizing the yttrium distribution, Corros. Sci. 159 (2019) 108145.
[33] W. Chen, L. He, Y. Guo, X. Shan, J. Li, F. Guo, X. Zhao, N. Ni, P. Xiao, Effects of reactive element oxides on the isothermal oxidation of β-NiAl coatings fabricated by spark plasma sintering, Surf. Coat. Technol. 357 (2019) 322–331.
[34] W. Chen, X. Shan, Y. Guo, J. Li, Z. Zou, F. Guo, X. Zhao, P. Xiao, The effect of reactive element species and concentrations on the isothermal oxidation of β-NiAl coating fabricated by spark plasma sintering, Surf. Coat. Technol. 357 (2019) 841–848.
[35] Y. Chen, X. Zhao, M. Bai, L. Yang, C. Li, L. Wang, J.A. Carr, P. Xiao, A mechanistic understanding on rumpling of a NiCoCrAlY bond coat for thermal barrier coating applications, Acta Mater. 128 (2017) 31–42.
[36] L. Yang, Z. Zou, Z. Kou, Y. Chen, G. Zhao, X. Zhao, F. Guo, P. Xiao, High temperature stress and its influence on surface rumpling in NiCoCrAlY bond coat, Acta Mater. 139 (2017) 122–137.
[37] J. Lu, Y. Chen, H. Zhang, N. Ni, L. Li, L. He, R. Mu, X. Zhao, F. Guo, Y/Hf-doped AlCoCrFeNi high-entropy alloy with ultra oxidation and spallation resistance, Corros. Sci. (2020) 108426.
[38] C. Wagner, Theoretical analysis of the diffusion processes determining the oxidation rate of alloys, J. Electrochem. Soc. 99 (1952) 369–380.
[39] F. Gesmundo, F. Viani, Y. Niu, et al., The transition from the formation of mixed scales to the selective oxidation of the most-reactive component in the corrosion of single and two-phase binary alloys, Oxid. Met. (1993) 373.
[40] H.E. Evans, M.P. Taylor, Diffusion cells and chemical failure of MCrAlY bond coats in thermal-barrier coating systems, Oxid. Met. 55 (2001) 17–34.
[41] Y. Chen, X. Zhao, P. Xiao, Effect of microstructure on early oxidation of MCrAlY coatings, Acta Mater. 159 (2018) 150–162.
[42] G.-H. Meng, H. Liu, P.-Y. Xu, G.-R. Li, T. Xu, G.-J. Yang, C.-J. Li, Superior oxidation resistant MCrAlY bond coats prepared by controlled atmosphere heat treatment, Corros. Sci. 170 (2020) 108653.
[43] D.R. Clarke, C.G. Levi, Materials design for the next generation thermal barrier coatings, Annu. Rev. Mater. Res. 33 (2003) 383–417.
[44] A. Chyrkin, N. Mortazavi, M. Halvarsson, D. Grüner, W.J. Quadakkers, Effect of thermal cycling on protective properties of alumina scale grown on thin Haynes 214 foil, Corros. Sci. 98 (2015) 688–698.
[45] H.-Z. Yang, J.-P. Zou, Q. Shi, M.-J. Dai, S.-S. Lin, W. Du, L. Lv, Analysis of the microstructural evolution and interface diffusion behavior of NiCoCrAlYTa coating in high temperature oxidation, Corros. Sci. 153 (2019) 162–169.
[46] Z. Liu, W. Gao, K.L. Dahm, F. Wang, Oxidation behaviour of sputter-deposited Ni–Cr–Al micro-crystalline coatings, Acta Mater. 46 (1998) 1691–1700.
[47] J.A. Nychka, D.R. Clarke, Quantification of aluminum outward diffusion during oxidation of FeCrAl alloys, Oxid. Met. 63 (2005) 325–352.
[48] F.A. Golightly, The relationship between oxide grain morphology and growth mechanisms for Fe-Cr-Al and Fe-Cr-Al-Y alloys, J. Electrochem. Soc. 126 (1979) 1035.
[49] F.A. Golightly, F.H. Stott, G.C. Wood, The influence of yttrium additions on the oxide-scale adhesion to an iron-chromium-aluminum alloy, Oxid. Met. 10 (1976) 163–187.
[50] D. Li, H. Guo, D. Wang, T. Zhang, S. Gong, H. Xu, Cyclic oxidation of β-NiAl with various reactive element dopants at 1200°C, Corros. Sci. 66 (2013) 125–135.
[51] B.A. Pint, Experimental observations in support of the dynamic-segregation theory to explain the reactive-element effect, Oxid. Met. 45 (1996) 1–37.
[52] D.S. Balint, T. Xu, J.W. Hutchinson, A.G. Evans, Influence of bond coat thickness on the cyclic rumpling of thermally grown oxides, Acta Mater. 54 (2006) 1815–1820.
[53] D. Balint, J. Hutchinson, An analytical model of rumpling in thermal barrier coatings, J. Mech. Phys. Solids 53 (2005) 949–973.
[54] V.K. Tolpygo, D.R. Clarke, Surface rumpling of a (Ni, Pt)Al bond coat induced by cyclic oxidation, Acta Mater. 48 (2000) 3283–3293.
[55] M.-H. Tsai, C.-W. Wang, C.-W. Tsai, W.-J. Shen, J.-W. Yeh, J.-Y. Gan, W.-W. Wu, Thermal stability and performance of NbSiTaTiZr high-entropy alloy barrier for copper metallization, J. Electrochem. Soc. 158 (2011) H1161.
[56] C.-Y. Hsu, C.-C. Juan, W.-R. Wang, T.-S. Sheu, J.-W. Yeh, S.-K. Chen, On the superior hot hardness and softening resistance of $AlCoCr_xFeMo_{0.5}Ni$ high-entropy alloys, Mater. Sci. Eng. A. 528 (2011) 3581–3588.
[57] K.Y. Tsai, M.H. Tsai, J.W. Yeh, Sluggish diffusion in Co–Cr–Fe–Mn–Ni high-entropy alloys, Acta Mater. 61 (2013) 4887–4897.
[58] M.C. Gao, J.-W. Yeh, P.K. Liaw, Y. Zhang, High-entropy Alloys Fundamentals and Applications, Springer International Publishing, 2016.
[59] Q. Li, W. Chen, J. Zhong, L. Zhang, Q. Chen, Z.-K. Liu, On sluggish diffusion in fcc Al–Co–Cr–Fe–Ni high-entropy alloys: an experimental and numerical study, Metals 8 (2017) 16.
[60] D. Miracle, J. Miller, O. Senkov, C. Woodward, M. Uchic, J. Tiley, Exploration and development of high entropy alloys for structural applications, Entropy 16 (2014) 494–525.
[61] R.J. Christensen, V.K. Tolpygo, D.R. Clarke, The influence of the reactive element yttrium on the stress in alumina scales formed by oxidation, Acta Mater. 45 (1997) 1761–1766.
[62] J. Liu, J.W. Byeon, Y.H. Sohn, Effects of phase constituents/microstructure of thermally grown oxide on the failure of EB-PVD thermal barrier coating with NiCoCrAlY bond coat, Surf. Coat. Technol. 200 (2006) 5869–5876.